EES Batteries

Accepted Manuscript

This article can be cited before page numbers have been issued, to do this please use: S. Liu, B. Wang, S. Tian, B. Wang, Y. Wang, Z. Rong, G. Zhang, J. Zhang, C. Li, T. Wang, Z. Liu, X. Guo, L. Gu, J. Huang and H. Yu, *EES Batteries*, 2026, DOI: 10.1039/D6EB00073H.

View Article Online
DOI: 10.1039/D6EB00073H

Manganese-rich layered oxides (Mn-LLOs) are regarded as a "holy grail" for next-generation lithium-ion batteries due to their high energy density and cost-effectiveness. However, their commercial deployment is hindered by a persistent trade-off where lattice stability is typically compromised by strategies intended to accelerate ion transport. Here, a generalizable "dual defect" engineering strategy is introduced to effectively decouple this conflict. Through an aluminum phosphate composite approach, twin-boundary interfaces and oxygen vacancies are simultaneously encoded into the crystal lattice. Inter-slab spacing is widened by twin boundaries to facilitate rapid transport, while migration barriers are drastically lowered from 0.45 eV to 0.29 eV by bulk oxygen vacancies. Structural "imperfections" are thus converted into functional assets, ensuring both high rate performance and cycle durability. Consequently, an 18% enhancement in rate capability is achieved in practical 250 mAh pouch cells, and 90.7% capacity retention is maintained after 1000 cycles at 45 °C. A generalizable, defect-centric blueprint for sustainable, cobalt-free batteries is established, demonstrating that the full potential of Mn-based cathodes can be unlocked by precise lattice tailoring.

View Article Online
DOI: 10.1039/D6EB00073H

ARTICLE

Dual defect engineering tailored Li^+ diffusion kinetics for sustainable Mn-based composite-structure cathode materials

Received 00th January 20xx,
Accepted 00th January 20xx

DOI: 10.1039/x0xx00000x

Shiqi Liu[abc], Boya Wang[d], Shaoze Tian[abc], Bo Wang[e], Yulong Wang[abc], Zhaoyu Rong[e], Guanhua Zhang[f], Jinjin Zhang[g], Chenghan Li[abc], Tian Wang[abc], Ziliang Liu[abc], Xianwei Guo*[abch], Lin Gu*[d], Jianyu Huang[e] and Haijun Yu*[abc]

Manganese-rich layered oxides are promising cathodes for next-generation lithium-ion batteries, yet their practical deployment is hindered by sluggish Li^+ diffusion, voltage fade, and Mn dissolution triggered by lattice instability. To date, a generalizable design principle that simultaneously accelerates Li^+ transport remains and suppresses electrochemical fading elusive. Here a dual-defect engineering strategy that concurrently generates twin-boundary interfaces and oxygen vacancies in phosphate-composite Mn-LLO crystal lattices was introduced. The twin boundary defect enlarges Li^+ transport channels within the Li slabs, while oxygen vacancies efficiently lower Li^+ migration barriers, guaranteeing the fast Li^+ transport and competitive electrochemistry. The engineered Mn-based composite cathode delivers 18% rate enhancement at 1C and 90.7% capacity retention after 1000 cycles at 45 °C in 250 mAh pouch cells. Post-mortem analysis reveals uniform Mn/Ni redox and suppressed electrolyte decomposition in the phosphate-composite cathode system. This scalable approach is compatible with commercial Mn-based oxide cathodes and can be extended to other layered oxide systems, offering a defect-centric pathway toward high-stability batteries.

Introduction

The cost, energy density, and cycle life are currently the top concerns for the public and research communities for the electrochemical energy storage (EES) systems powered by lithium-ion batteries (LIBs) technology.[1, 2] Among the cathode candidates for the battery-enabled EES systems, despite the economic viability, safety and long-time cycling stability, lithium iron phosphate ($LiFePO_4$, LFP) is still confined to niche application scenarios by its intrinsically low energy density and poor low-temperature kinetics. In contrast to Fe-based cathode driven EES systems, manganese-based (Mn-based) cathode materials are rapidly emerging as formidable contenders in cathode materials for the next-generation EES devices, leveraging the earth-abundance of Mn to secure intrinsically low raw-material costs while simultaneously offering high energy density and competitive cycling stability that together position them as a viable alternative to incumbent technologies.[3-5] Among various Mn-based cathode materials such as Mn-based Li-rich layered oxides (Mn-LLOs), Mn-based spinel oxides (LMO) and lithium manganese iron phosphates (LMFP), Mn-LLOs offers the highest energy density and shows the structural regulation potentials for EES systems to guarantee the long-cycle stability.[6]

Rather than triggering oxygen participation, our strategy intentionally keeps the Li_2MnO_3 domains in an unactivated state (<4.4 V) to function as uniformly dispersed, inert stabilizing functional units throughout the bulk lattice. This crystal domain engineering fully stabilizes the Mn-LLO cathode, balancing the overall electrochemical performance solely through the highly stable cationic redox contribution of the $LiTMO_2$ domains. Apart from tailoring the activation process and proportions of Li_2MnO_3 and $LiTMO_2$ crystal domains in Mn-LLOs, the electrochemical performance of Mn-LLOs could achieve elevated energy density, prolonged cycle lifetime, and robust electrochemical behavior over a broad thermal window than those of the Mn-based analogues.[7] Nevertheless, critical bottlenecks persists those rate capability and the electrochemical stability remain shy of practical thresholds.[6, 8] Despite the well-ordered structure design in the previous cathode systems, introducing disordered structures in the bulk lattices could also provide opportunities for enhancing the structural reversibility and kinetics.[9, 10] Partially disordered δ

[a.] Institute of Advanced Battery Materials and Devices, College of Materials Science and Engineering, Beijing University of Technology, Beijing 100124, China. E-mail: hj-yu@bjut.edu.cn, xwguo@bjut.edu.cn
[b.] Institute of Gongda-Guochuang Advanced Battery Materials and Devices, Beijing, 100176, P. R. China.
[c.] State Key Laboratory of Materials Low-Carbon Recycling, Institute of Matter Science, Beijing University of Technology, Beijing 100124, China.
[d.] Beijing National Center for Electron Microscopy and Laboratory of Advanced Materials, School of Materials Science and Engineering, Tsinghua University, Beijing 100084, China. E-mail: lingu@mail.tsinghua.edu.cn
[e.] Clean Nano Energy Center, State Key Laboratory of Metastable Materials Science and Technology, Yanshan University, Qinhuangdao 066000, China.
[f.] State Key Lab of Chemical Reaction Dynamics, Dalian Institute of Chemical Physics, Chinese Academy of Sciences, Dalian 116023, P.R. China.
[g.] Shanghai Synchrotron Radiation Facility, Shanghai Advanced Research Institute, Chinese Academy of Sciences, Shanghai, China.
[h.] Beijing Create Energy & Benefit Future Co., Ltd., Beijing 100176, China.
† Footnotes relating to the title and/or authors should appear here.
Supplementary Information available: [details of any supplementary information available should be included here]. See DOI: 10.1039/x0xx00000x

phase with short coherence length in spinel-like lattice environment was formed from the fully disordered rocksalt phase, showing not only the superior energy density and rate capability, but also the no voltage decay feature.[10] Besides, applied with special low-potential activation method, the structure of Mn-LLO cathode could be accurately controlled to generate the Li/Mn cationic disordered structure, resulting in the enhanced reversibility of oxygen activities and excellent rate and cycling performance.[11]

In this work, the long-standing trade-off between rate capability and cycling stability in Mn-LLO cathodes is demonstrated, which can be effectively decoupled through a targeted dual defect engineering approach. Instead of treating structural defects as detrimental, the aluminum phosphate composition is utilized to tailor the lattice environment, creating a coexistence of twin boundaries and oxygen vacancies. This specific configuration serves a dual purpose: it facilitates rapid Li^+ diffusion through expanded lattice channels and stabilizes the redox framework against aggressive electrolyte side reactions. Consequently, the engineered cathode exhibits superior electrochemical resilience and kinetic efficiency in practical pouch cells. The advantage of introducing phosphates to construct structural defects in Mn-LLOs is not applicable to the energy-storage low-voltage cathode systems but is also potentially suitable to typical ultrahigh-energy Mn-LLOs.

Structural of phosphate-composite Mn-based cathode

The Mn-LLO cathode was synthesized by the hydroxide precursor sintered with lithium carbonate, then $AlPO_4$ (AP) additive was introduced into Mn-LLO cathode material by the mechanofusion technique accompanied with the heating process (denoted as Mn-LLO-AP). Fig. 1a and S1 show the synchrotron-based X-ray diffraction (SXRD) patterns and Rietveld refinement with two-phase model results of the as-prepared cathode materials, indicating the presence of the major $LiTMO_2$ crystal domain with space group of $R\bar{3}m$ and minor Li_2MnO_3 crystal domain with space group of C/2m in the lattice (Table S1 and S2).[3, 4] Corresponding to the refinement result, the Li/Ni mixing phenomenon would slightly increase from 6.0(7)% to and 8.1(5)%, indicating the elemental induced structural rearrangement in the local structure of the phosphate-composite cathodes. In addition to the structural changes, the morphologies of the secondary aggregate particles in Mn-LLO-AP show the dense and smooth primary particle arrangement at the surface (insets of Fig. 1a). In addition, the oxygen occupancy refined from the SXRD data is 0.94, showing the phosphate-incorporate induced the oxygen vacancy defect in the crystal lattice. Due to the detective sensitivity of light elements, neutron powder diffraction (NPD) is performed onto Mn-LLO-AP. The NPD refinement results also show the similar oxygen occupancy results with the SXRD data (Fig. 1b), indicating the potential point defect at the oxygen sites.

Results and discussion

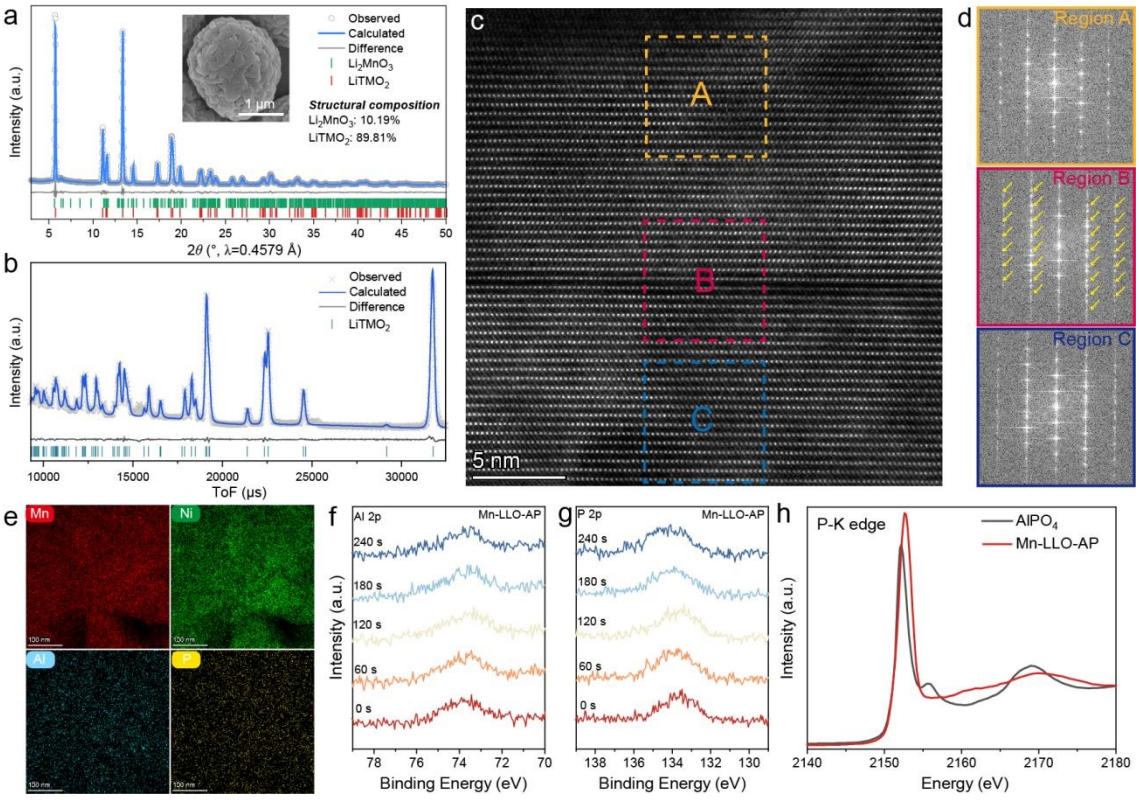

Fig. 1 | Crystallographic and elemental information for a series of phosphate-composite Mn-based cathode materials. a, SXRD Rietveld refinement result and **b,** NPD refinement result of Mn-LLO-AP cathode. **c,** High-resolution HAADF-STEM image of Mn-LLO-AP cathode material. **d,** FFT patterns of selected regions

of Mn-LLO-AP in the HAADF-STEM. **e,** Elemental mapping images collected under the TEM mode. **f,** Al 2p and **g,** P 2p XPS results collected from the pristine Mn-LLO-AP cathode with different Ar^+ sputtering times. **h,** P K-edge XANES spectra of $AlPO_4$ and Mn-LLO-AP samples.

View Article Online
DOI: 10.1039/D6EB00073H

To further investigate the bulk atomic structure of Mn-LLO-AP the high-angle annular dark-field (HAADF) scanning transmission electron microscopy (STEM) images were collected in the focused-ion beam (FIB) processed samples. The atomic structure of Mn-LLO-AP cathode material is shown in Fig. 1c and S2. Apart from the typical O3-type configuration in Regions A and C, twinning structure and boundary interface are presented in Region B inside the Mn-LLO-AP bulk phase.[12] This crystal defect can only be observed by extra bright spots generated in the fast Fourier transform (FFT) pattern of Region B (Fig. 1d and S3). And the surface of Mn-LLO-AP is observed to be the typical layered structure without apparent Li/TM mixing (Fig. S2a). In addition, the HAADF-STEM image project along the [001] zone axis shows the dispersive $LiMn_6$ hexatomic rings in the crystal lattice due to the small proportion of Li_2MnO_3 crystal domain in Mn-LLO-AP (Fig. S2b).[13-15]

As illustrated in Figs. 1e and S4, the energy-dispersive spectroscopy (EDS) maps show elemental distribution in the Mn-LLO-AP cathode cross-section particles. The Mn, Ni, Al, O and P elements all show the uniform distribution behavior inside the particles. In addition to the EDS results, the X-ray photoelectron spectroscopy (XPS) technique is also facilitated with Ar^+ sputtering processes to measure the elemental distribution by depth. As shown in Fig. 1f,g, the binding energies at ~73.8 eV and ~133.6 eV represent the Al 2p and P 2p signals in Mn-LLO-AP cathode particles. After 240 seconds Ar^+ sputtering, the intensity of these representative peaks show the same behavior without any shift in binding energy, suggesting the uniform Al and P elemental dispersion in the bulk phase of Mn-LLO-AP cathode material. The XPS spectra of Mn and Ni show the similar behaviors, indicating the unchanged chemical valence of these two materials from the surface to the bulk (Fig. S5). Furthermore, to scrutinize the P elemental chemical states and local environments in the phosphate-composite cathode materials, P K-edge X-ray absorption near-edge spectra (XANES) of AP and Mn-LLO-AP samples are collected through the tender X-ray absorption spectroscopy (XAS) technique. The absorption edges at the energy of 2151.5 eV of AP and Mn-LLO-AP show the overlapped behavior, indicating the similar valence of P in the phosphate additive and the as-prepared cathode material (Fig. 1h). Besides, the differences in peaks at 2152.5 and 2169 eV represent the tiny distortion of the P–O bonding in the species of PO_4 polyanion structure, indicating the changes of P local environment in the layered structure of Mn-LLO cathode materials after the heating processes.[16, 17] The peak at the photon energy of 138.6 eV harvested by the soft XAS (SXAS) technique also reflects PO_4^{3-} polyanionic signal in Mn-LLO-AP (Fig. S6).[18]

Electrochemistry

The electrochemical performance of Mn-LLO and Mn-LLO-AP cathode materials has been analysed through coin cells and pouch cells setups (Fig. 2). Within the testing voltage range of 2.5-4.4 V, the initial reversible capacity of Mn-LLO and Mn-LLO-AP are 161 and 165 mAh g^{-1} at 0.1C and 25 °C (Fig. 2a, solid lines), respectively, showing the similar Li^+ diffusion capability at low cycling rate. However, upon the rate of 1C, the voltage profiles and reversible capacities present quite discrepancies in these cathode materials (Fig. 1a, dot lines). The charging profile of Mn-LLO shows a slope shape beginning at ~3.9 V. Yet after phosphate incorporation, both onset charging and discharging voltages in the profile is reduced ~0.1 V, which is also reflected in the dQ/dV plots (Fig. S7), resulting in 9% energy efficiency improvement (from 78% to 87%). This kinetic behavior is also scrutinized through the galvanostatic intermittent titration technique (GITT) measurements for three cathode materials at 0.1C in the room temperature (Fig. 2b). According to the voltage profiles and the calculated Li^+ diffusion coefficients, the largest difference lies in the beginning and ending of charging and discharging with ~87% and ~49% variation, respectively, indicating the sluggish Li^+ migration at the Li-rich states of the structure and the phosphate-composite strategy could efficiently enhance the Li^+ kinetics. Thus, the reversible capacity at 1C could be raised from 123.4 mAh g^{-1} for Mn-LLO to 145.5 mAh g^{-1} for Mn-LLO-AP (Fig. 2a). The leak current test is also performed after the formation process, showing the small leakage current with enhanced interphase stability for Mn-LLO-AP cathode (Fig. S8). The distribution of relaxation time (DRT) profiles calculated from the electrochemical impedance spectroscopy (EIS) test for these three cathodes indicate the stable cathode-electrolyte interface layers in phosphate-composite cathodes (Fig. S9).[19]

View Article Online
DOI: 10.1039/D6EB00073H

ARTICLE

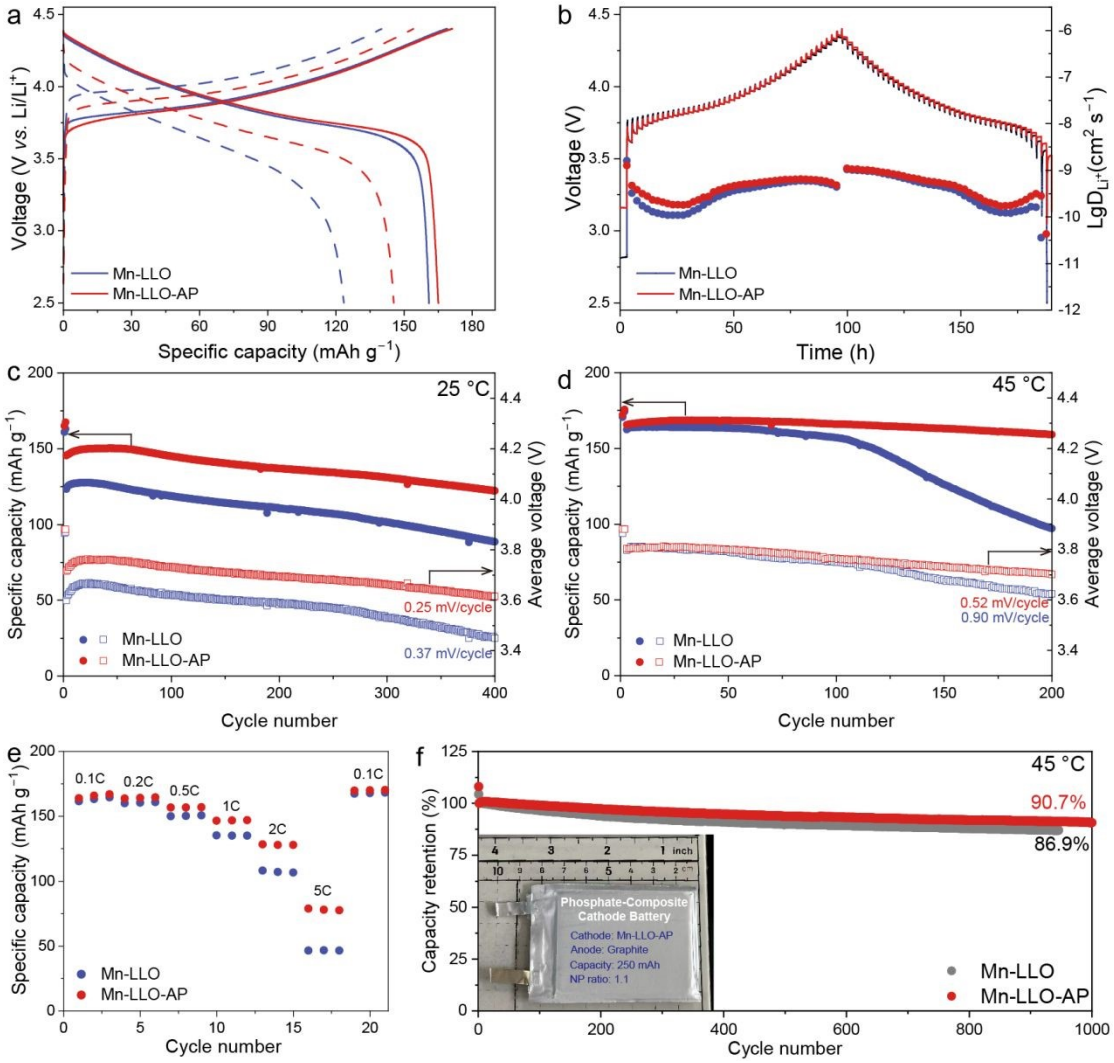

Fig. 2 | Electrochemical performance tests for Mn-LLO and Mn-LLO-AP cathodes. a, Initial voltage profiles at 0.1C (solid lines) and 1C (dot lines). **b,** Charging/discharging profiles under the GITT mode and Li^+ diffusion coefficients calculated from the GITT results. Cycle and discharged voltage stability tested at **c,** 25 °C and **d,** 45 °C. **e,** Rate capability test. **f,** Cycle performance test at 45 °C in the pouch cells.

The capacity and voltage stability versus cycling numbers of Mn-LLO and Mn-LLO-AP is tested at different temperatures (Figs. 2c,d). After 400 cycles at 25 °C, the capacity could retain 71.5%, 83.8%in Mn-LLO and Mn-LLO-AP cathodes, respectively. But the specific capacity of the unmodified Mn-LLO cathode material would drop quickly at elevated temperature in the half cell, indicating the aggravate side reactions between the electrodes and electrolytes. However, stable electrochemical operation is generated in the Mn-LLO-AP cathode with 95.8% of capacity retention, respectively. Furthermore, the average discharge voltage could also be stabilized after phosphate incorporation, showing 0.25 mV/cycle (400 cycles in 25 °C) and 0.5 mV/cycle (200 cycles in 45 °C) for Mn-LLO-AP cathode material in Figs. 2c,d. In addition to the stability tests, the rate capability of these three cathodes also shows in Fig. 2e, displaying the enhanced capacity of phosphate incorporated Mn-based cathode at higher rates with more than 78 mAh g^{-1} at 5C. Finally, 250 mAh pouch cells are also assembled with Mn-LLO and Mn-LLO-AP cathodes and graphite anode to verify the electrochemical stability practically and precisely (Figs. 1f and S10). Compared to Mn-LLO cathode, Mn-LLO-AP shows the excellent electrochemical behaviors both in 25 and 45 °C with ~103.8% and 90.7% capacity retention, indicating the fully potential for the long-life energy storage applications.

View Article Online
DOI: 10.1039/D6EB00073H

ARTICLE

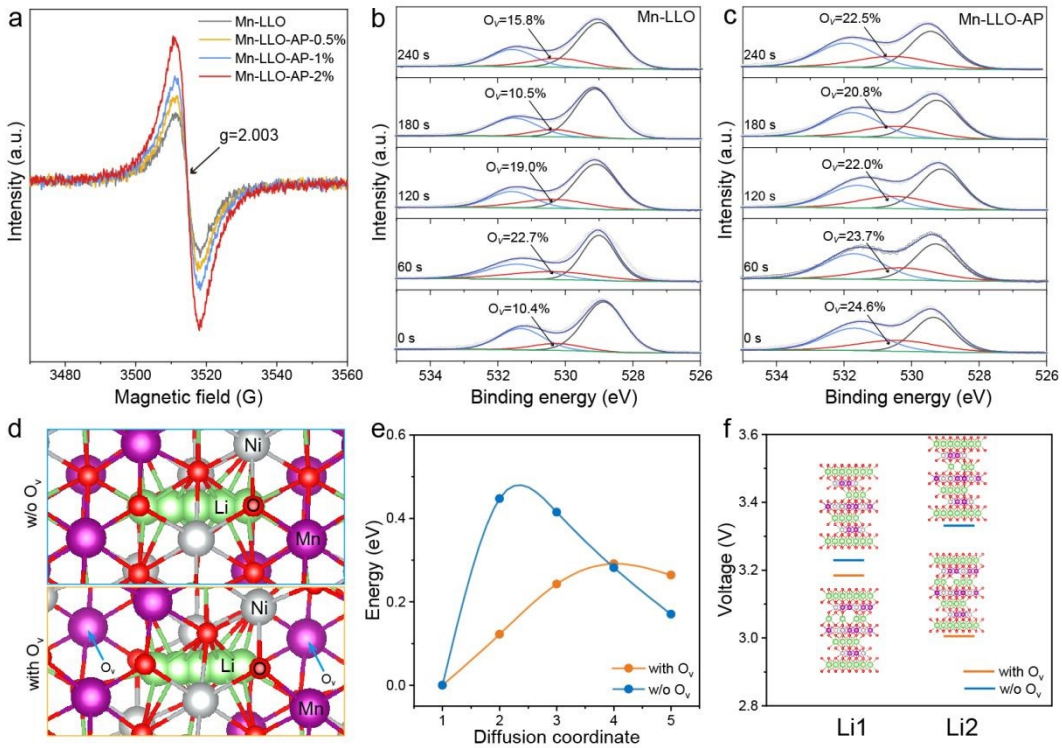

Fig. 3|The oxygen vacancy defect and its electrochemical behaviors. a, The EPR spectra of the Mn-based composite-structure cathode with different AP weight ratios. O 1s XPS spectra with different Ar^+ sputtering times of **b,** Mn-LLO and **c,** Mn-LLO-AP cathodes. **d,** The crystal model with different O_V defects and the Li^+ migration paths. **e,** The migration barrier of Li^+ in different paths. **f,** The delithiation voltages at different delithiation content with various O_V defects.

Impact of oxygen vacancy defect on Li^+ migration

In addition to the stability optimization, the rate performance is also influenced through the phosphate decoration. Due to the secondary sintering process with phosphate precursors, the lattice oxygen of Mn-based cathodes would be effected. Electron paramagnetic resonance (EPR) technique could detect the unpaired electrons in the atoms and molecules, which can provide the structural information especially the vacancies in electrode materials. To investigate the oxygen vacancy (O_V) behaviors, EPR spectra are acquired at room temperature Mn-LLOs cathode materials with different AP addition (0.5, 1, and 2% in weight ratio). EPR signals with a g value of 2.003 shown in Fig. 3a confirm the growth trend of total O_V with the increased AP addition. Compared to the pristine Mn-LLO cathode, the O 1s XPS spectra of Mn-LLO-AP with different Ar^+ sputtering times show the higher content of O_V peak signal than at the binding energy of 530.8 eV (Fig. 3b,c). Abovementioned characterizations suggest the O_V in largely uniformed distributed in the lattice structure of Mn-LLO-AP cathode. During heat treatment, Al dopes into the Mn-LLO lattice via elemental interdiffusion and substitutes host ions.[20] To maintain charge equilibrium, this triggers the valence adjustment of surrounding ions. Concurrently, the reaction between $AlPO_4$ and surface residual alkalis facilitates near-surface Li extraction. These mechanisms collectively induce a local excess of positive charge, driving the release of lattice oxygen and the formation of oxygen vacancies to preserve charge neutrality. Through the formation of oxygen vacancy defects in the crystal lattice of Mn-LLO-AP compound, the pre-introduced oxygen vacancies could act as a structural buffer to mitigate subsequent oxygen loss.[21-23] However, the excessive accumulation of oxygen vacancies continuously and uncontrollably generated during electrochemical cycling would inevitably destabilizes the oxide framework and lead to irreversible oxygen loss.

Accordingly, the density functional theory (DFT) calculation is performed with different O_V defects content in the Mn-LLO cathode model. As illustrated in Fig. 3d, the Li^+ migration path shows in different O_V models (with and without O_V), showing the oxygen dumbbell hop mechanism due to the absent of Li divacancy.[24, 25] And thus, the Li^+ migration energy barrier profiles show a single-peak characteristic, and the highest calculated diffusion energy barrier is 0.291 eV in the O_V model, which is obvious lower than that of O intact model for 0.448 eV

View Article Online
DOI: 10.1039/D5EE00775H

(Fig. 3e). This indicates that the formation of oxygen vacancies could facilitate the Li^+ diffusion, resulting in the better rate capability of Mn-LLO-AP than that of Mn-LLO in electrochemistry. In addition, aforementioned sluggish Li^+ migration phenomenon reflected from the voltage hysteresis and onset voltage profile at the Li-rich states (low and high states of charge) of the layered structure is also verified through calculated voltages in different delithiation sites of intact and O_V models (Fig. 3f). Once the oxygen vacancy is formed in the crystal lattice, the delithiation potential could reduce from 3.331 V to 3.005 V, consistent with initial charge profiles at 1C (Fig. 2a), indicating the enhanced Li^+ diffusion ability in this lattice defect structural system.

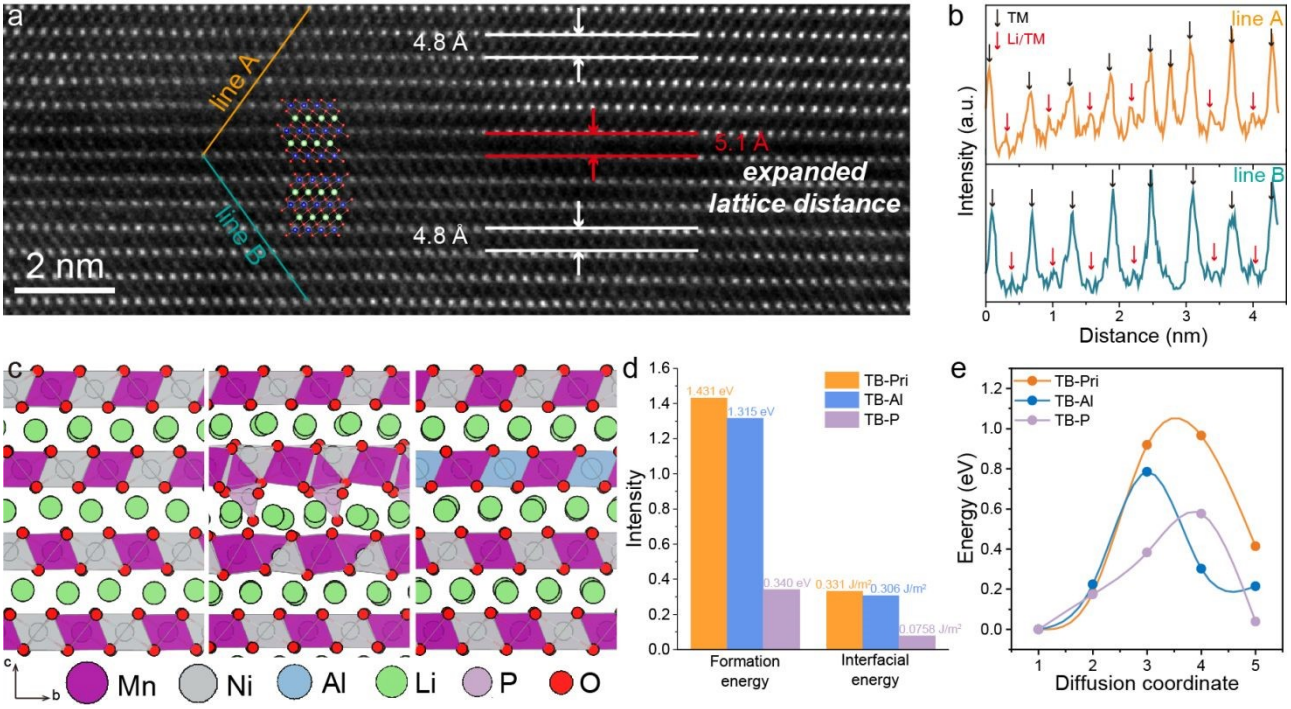

Fig. 4 | The twin boundary defect engineering in Mn-based composite-structure cathode systems. a, The enlarged HAADF-STEM image of the twin boundary defect in Mn-LLO-AP cathode. **b,** The line intensity of the selected regions neighbouring the twin boundary defect. **c,** The crystal model of the twin boundary defect in Mn-LLO-AP cathode with different elements introduction. **d,** The formation energies and interfacial energies of the twin boundary defect in the composite-structure cathode. **e,** The Li^+ diffusion barriers of different Li^+ migration models.

Impact of twin boundary defect on Li^+ migration

Another structural characteristic exists in the atomic local environment of Mn-LLO-AP cathode material, showing the prominent twin boundary defect feature (Fig. 4a). As demonstrated in Fig. 4a, one of the obvious feature in the Mn-LLO-AP lattice is the enlarged lattice distance of 5.1 Å at the interface, which is different from the typical 4.8 Å lattice distance in O3 structure. This feature would provide sufficient Li^+ migration paths and be benefit to the ion-transport kinetics during (de)lithiation processes. Another feature observed in the HAADF-STEM image and the line intensity plots (Fig. 4b) shows bright contrasts in the Li layers and enhanced line intensity at the red-arrow positions, respectively, indicating the Li/TM mixing behavior in the lattice. To assess the reaction feasibility and structural stability within different elemental introduced layered cathode systems, theoretical twinning crystal model construction and DFT calculations (Figs. 4d,e) are applied for the verifying the formation mechanism of this twinning characteristic in phosphate decorated Mn-LLO cathode material. The twinning structure is firstly constructed within the Li-Mn-Ni-O layered oxide system (Fig. 4c, left, TB-Pri). Then, P and Al elements are introduced into the twinning structure individually (Fig. 4c, middle and right, TB-Al and TB-P, respectively). The P-O polyhedra is located in the tetrahedral site in the Li layers and Al atoms are inclined to occupy the octahedral site in the TM layers.[20, 26]

The formation energy of the twinning structure with various doping elements and the interfacial energy of the twin boundary show that the P introduction can result in the lowest value, indicating that the twinning structure could be formed easily and the twin boundary could be reinforced with the phosphorus element incorporation. In addition, the crystal releases the strain induced by phosphorus incorporation through slip or twinning deformation, creating twin boundaries. Therefore, the twin boundary defect engineering could be formed readily in the phosphate-composite Mn-LLO-AP cathode system theoretically. Apart from the expanded lattice distance at the twin boundary enhanced kinetics in Mn-LLO-AP cathode, the elemental heterogeneity could also be boosted. Fig. 4e shows the Li ion migration energy barrier curves of TB-Pri, TB-Al, and TB-P, demonstrating the decreased diffusion energy barrier from 0.965 eV to 0.7849 eV and 0.5754 eV, respectively. These results suggest that the formation of twin boundary defects and the elemental introduction could both augment the Li ion migration kinetics and construct a high-rate Mn-LLO cathode material.

View Article Online
DOI: 10.1039/D6EB00073H

ARTICLE

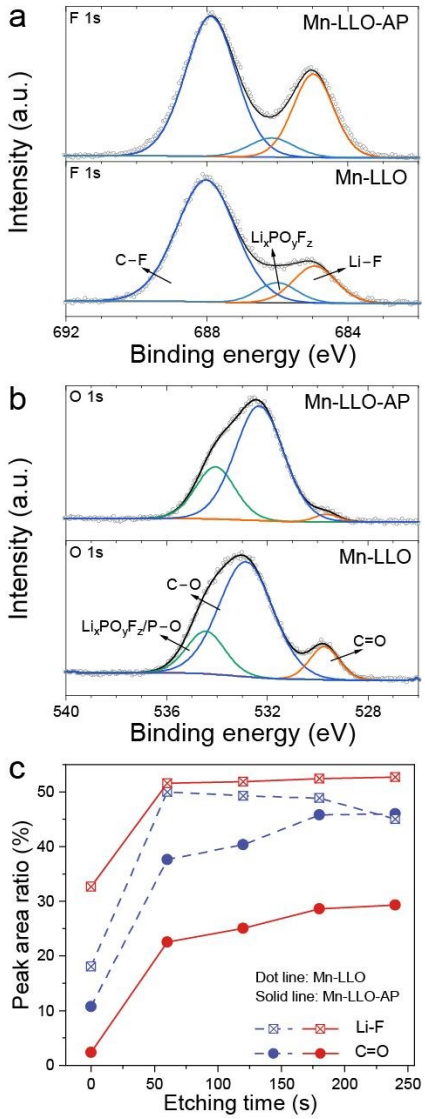

Fig. 5 | The structural-activity relationships between residual protons and the electrochemical behaviors. XPS spectra of Mn-LLO and Mn-LLO-AP cathodes of **a,** F1s and **b,** O1s. **c,** Concentration variations of the C=O and Li-F chemical interactions calculated in C 1s and F 1s, respectively. The interaction information are shown in dot lines and solid lines for Mn-LLO and Mn-LLO-AP cathodes, respectively.

Elemental stability in Mn-based cathodes

Due to the enhancement of the electrochemical performance in the phosphate-composite cathode, the quality of the cathode electrolyte interface (CEI) film form during Mn-LLO and Mn-LLO-AP cathode cycling is scrutinized by the surface-sensitive XPS technique. Figs. 5a,b show the F 1s and O 1s XPS spectra of these cathode materials after 100 cycles. It could be observed that the peak at binding energy of 684.8 eV could be deconvoluted and be considered as the LiF species in the CEI. This inorganic chemical could endow the robustness of the interface and ensure the highly stable mechanical properties during electrochemistry. In addition to the inorganic species, organic fingerprints could be measured through the O 1s XPS spectra, showing the C=O signal at the binding energy of 529.8 eV. This feature represents to the decomposition of the solvent solutions from the organic electrolytes, and excessive degradation harms the steady operation of the battery systems. Accordingly, Mn-LLO-AP cathode shows the highest peak intensity in the F 1s spectra (Fig 5a) and the lowest peak signal in the O 1s spectra (Fig. 5b), indicating the abundance of LiF species at the interface and the integrity of the electrolyte.[4, 27] Furthermore, Ar^+ sputtered XPS spectra are also performed for these cathodes and the concentration variation of different species is summarized in Fig. 5c. Similar to the environment of outer layer in the CEI film, the amount of LiF and C=O species in Mn-LLO-AP suggests the high robust film property and the decreased electrolyte by-products. In addition to the XPS technique, TOF-SIMS information is also collected in these three cathode materials after 50 cycles (Fig. S11). According to the 3D rendering images and the TOF-SIMS intensity depth profiles of selected LiF^-, C_2HO^-, and PO_3^- fragments in these electrodes, the LiF^- fragment is largely prominent in proportion, reinforcing the feature of talented chemical species in the Mn-LLO-AP cathode materials.

Due to the enhanced electrochemical stability and kinetics, the reaction homogeneity of the single particle and reversibility of chemical states would present different behaviors. X-ray photoemission electron microscopy (X-PEEM) technique is performed to observe the localized chemical information on single Mn-based oxide particle at the delithiation state.[28] Fig. 6a shows the Mn chemical contrast maps based on Mn L_3-edge stacks of Mn-LLO and Mn-LLO-AP at the initial 4.4 V delithiation state, respectively. Corresponding to the chemical contrast maps and the extracted XAS spectra (Fig. 6b), the oxidation states of Mn is inhomogeneous within and between the Mn-LLO and Mn-LLO-AP particles. Nevertheless, Mn-LLO owns the larger degree of reaction heterogeneity inside the particles than that of Mn-LLO-AP. In addition to the oxidation state of Mn, the O and Ni chemical states at different detected regions also reflect the similar reaction degree in the O K-edge and Ni L_3-edge of Mn-LLO and Mn-LLO-AP particles. These phenomenon indicate that the pristine Mn-LLO cathode suffers more underlying structural variation differences inside a single particle and experiences more dangers to be failure in electrochemical cycling. And the lattice oxygen stability in Mn-LLO-AP cathode is superior to that in Mn-LLO, indicating the potential for long-cycle performance for the phosphate-composite Mn-based cathode materials.

View Article Online
DOI: 10.1039/D6EB00073H

ARTICLE

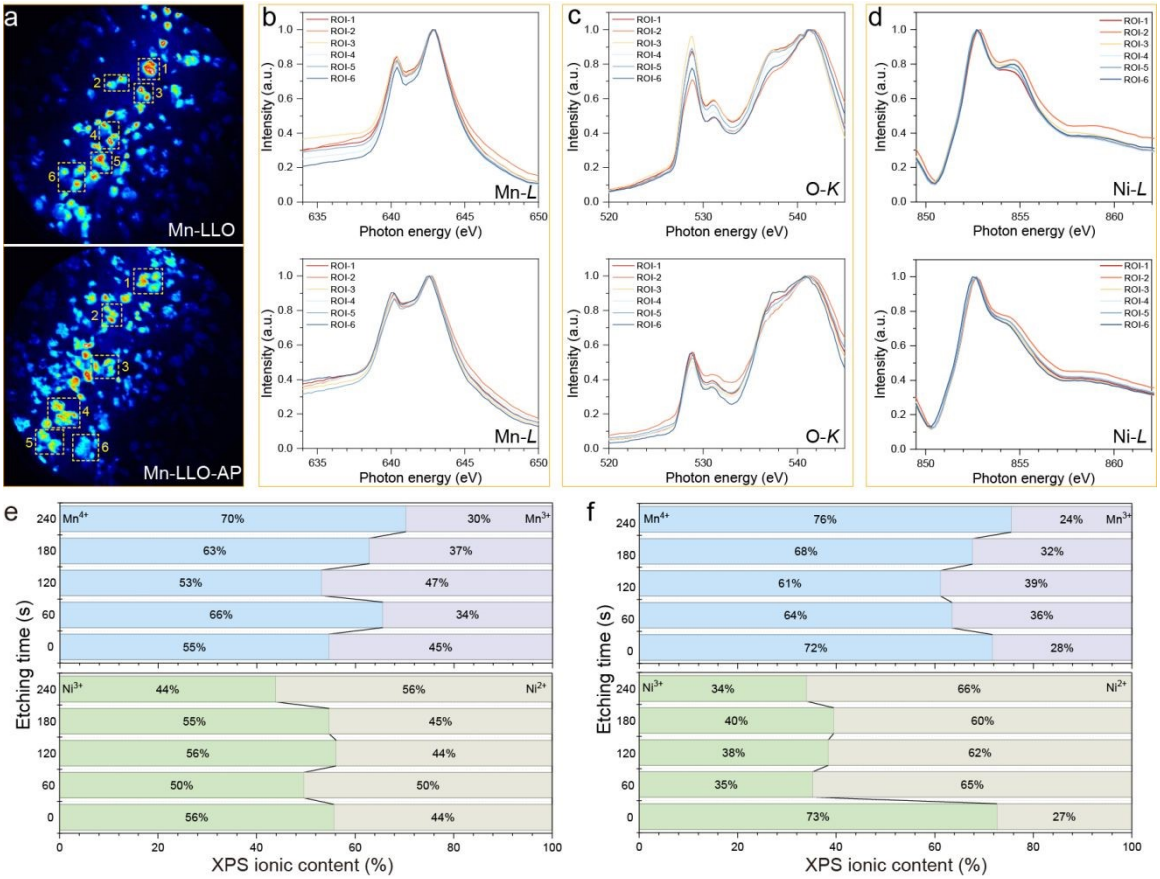

Fig. 6|The post-mortem analysis of Mn-based composite-structure cathode systems. a, X-PEEM Mn chemical mapping collected at the photon energy of 645 eV based on Mn L_3-edge stacks of Mn-LLO and Mn-LLO-AP cathode materials at the charged to 4.4 V state, respectively. **b,** Mn L_3-edge, **c,** O K-edge, and **d,** Ni L_3-edge XANES of Mn-LLO and Mn-LLO-AP cathode materials at the charged to 4.4 V state, respectively. Calculated XPS fitting peak ratios of $Mn^{4+/3+}$ and $Ni^{3+/2+}$ in **e,** Mn-LLO and **f,** Mn-LLO-AP cathode materials cycled after 100 cycles, respectively.

Apart from the single particle chemical states at the initial cycle, the average Mn and Ni valences after hundreds of cycles also be evaluated by the SXAS and XPS spectra technique with depth analysis. Mn and Ni L-edge spectra of Mn-LLO and Mn-LLO-AP at the pristine state show the similar chemical valence of +4 and +2, respectively (Figs. S12a,b). Yet the residual Li_2CO_3 signal at the photon energy of 533 eV in the Mn-LLO pristine state is eliminated through the phosphate-composite construction (Fig. S12c).[29] The average chemical valence of Mn and Ni after 100 cycles is harvested by fitting the $Mn^{4+/3+}$ and $Ni^{3+/2+}$ XPS depth information (Fig. 6). The etched Mn 2p and Ni 2p XPS spectra show that Mn-LLO-AP has the higher reversibility with the highest 76% of Mn^{4+} and 66% of Ni^{2+} than those of Mn-LLO cathode materials with ~60% of Mn^{4+} and ~50% of Ni^{2+} species. In addition, the ex situ SXAS spectra collected after 400 cycles show the similar oxygen chemical feature in the grain surface of Mn-LLO and Mn-LLO-AP cathodes (Fig. S13). These results reinforcing the evidence that the AP modified Mn-based cathode material could have both structural and chemical stability.

Conclusions

By simultaneously encoding twinning structure defect and oxygen vacancies defects into the energy-storage applicable Mn-based composite cathode, a generalizable, defect-centric route that resolves the long-standing trade-off between electrochemistry and Li^+ mobility is established. The twining boundaries expand the inter-slab spacing by 6 %, while the oxygen vacancies in the bulk lower the Li^+ migration barrier from 0.45 eV to 0.29 eV, yielding a nearly one-order-of-magnitude increase in diffusion coefficient. The engineered phosphate-composite Mn-based layered oxide cathode delivers 18 % higher rate capability at 1C, 90.7 % capacity retention at

45 °C, and no capacity decay at 25 °C after 1000 cycles in 250 mAh pouch cells. More broadly, encoding cooperative bulk defects offers a design blueprint that turns structural "imperfections" into functional assets, accelerating the transition to cobalt-free, Mn-based sustainable batteries.

Author contributions

Shiqi Liu: conceptualization, investigation, methodology, writing – original draft; Boya Wang: methodology, writing – review & editing; Shaoze Tian: investigation, methodology, data curation; Bo Wang: methodology, data curation; Yulong Wang: investigation, methodology, data curation; Zhaoyu Rong: methodology; Guanhua Zhang: methodology, data curation; Jinjin Zhang: methodology, data curation; Chenghan Li: methodology; Tian Wang: methodology; Xianwei Guo: writing – review & editing; Lin Gu: methodology, writing – review & editing; Jianyu Huang: methodology, writing – review & editing; Haijun Yu: supervision, funding acquisition, writing – review & editing.

Conflicts of interest

There are no conflicts to declare.

Data availability

The data supporting this article have been included as part of the ESI.†

Acknowledgements

This work was financially supported by the National Key R&D Program of China (No. 2022YFB2404400), the National Natural Science Foundation of China (No. 92572203, 92263206, U23A20577, 52372168, 52472181, U24A2065, and 22509104), "The Youth Beijing Scholars program" (No. PXM2021_014204_000023), the Fundamental Research Funds for Beijing Municipal Universities (312000546325001), and the Beijing Natural Science Foundation (No. 2222001). We thank the Shanghai Synchrotron Radiation Facility of BL09U (https://cstr.cn/31124.02.SSRF.BL09U) and BL16U (https://cstr.cn/31124.02.SSRF.BL16U1) for the assistance on X-PEEM and tender XAS measurements. We thank BL10B (https://cstr.cn/31131.02.HLS.PES) BL12B (XMCD, 31131.02.HLS.XMCD.a and 31131.02.HLS.XMCD.b) at the National Synchrotron Radiation Laboratory in Hefei for providing beam time of the SXAS measurements. We thank the staff members of the Multi-Physics Instrument (https://cstr.cn/31113.02.CSNS.MPI) at the China Spallation Neutron Source (CSNS) (https://cstr.cn/31113.02.CSNS), for providing technical support and assistance in data collection and analysis.

References

1. B. Dunn, H. Kamath and J.-M. Tarascon, *Science*, 2011, **334**, 928-935.
2. T. Jiang, D. Shen, Z. Zhang, H. Liu, G. Zhao, Y. Wang, S. Tan, R. Luo and W. Chen, *Nat. Rev. Clean Technol.*, 2025, **1**, 474-492.
3. Y. Wang, S. Liu, X. Guo, B. Wang, Q. Zhang, Y. Li, Y. Wang, G. Wang, L. Gu and H. Yu, *J. Mater. Sci. Technol.*, 2025, **207**, 266-273.
4. S. Liu, Y. Wang, D. Xiao, H. Du, R. Zhang, S. Tian, Y. Li, Y. Wang, J. Wang, G. Wang, Y. Li, S. Zhao, X. Guo and H. Yu, *Energy Storage Mater.*, 2025, **76**, 104151.
5. X. Zhang, S. Liu, B. Wang, G. Wang, H. Du, X. Wang, H. Zhang, S. Zhao, L. Wang and H. Yu, *Sci. China Chem.*, 2023, **67**, 87-105.
6. S. Liu, B. Wang, X. Zhang, S. Zhao, Z. Zhang and H. Yu, *Matter*, 2021, **4**, 1511–1527.
7. Y. Yang, Z. Zhang, S. Liu, B. Wang, J. Liu, Y. Ren, X. Zhang, S. Zhao, D. Liu and H. Yu, *Matter*, 2022, **5**, 3869-3882.
8. Y. Huang, C. Li, K. Zhang, Y. Tang, W. Tu, Y. Tian, J. Wang, Y. Yan, Y. Chen, Y. Zou, L. Li, B. Zhang, J. Bao, C. Ding, Y. Wang, T. Qiu, X. Sun, Y. Qiao and S. G. Sun, *Angew. Chem. Int. Ed.*, 2025, **64**.
9. S. Lee, S. Kang, Y. Choi, J. Kim, J. Yang, D. Han, K.-W. Nam, O. J. Borkiewicz, J. Zhang and Y.-M. Kang, *J. Am. Chem. Soc.*, 2024, **146**, 33845-33856.
10. Z. Cai, B. Ouyang, H.-M. Hau, T. Chen, R. Giovine, K. P. Koirala, L. Li, H. Ji, Y. Ha, Y. Sun, J. Huang, Y. Chen, V. Wu, W. Yang, C. Wang, R. J. Clément, Z. Lun and G. Ceder, *Nat. Energy*, 2023, **9**, 27-36.
11. M. Wang, C. Ke, H. Zhang, C. Hou, J. Chen, S. Liu and J. Wang, *Nano Lett.*, 2024, **24**, 12343-12352.
12. Y. Gong, J. Zhang, L. Jiang, J.-A. Shi, Q. Zhang, Z. Yang, D. Zou, J. Wang, X. Yu, R. Xiao, Y.-S. Hu, L. Gu, H. Li and L. Chen, *J. Am. Chem. Soc.*, 2017, **139**, 4274-4277.
13. L. Wang, S. Zhao, B. Wang and H. Yu, *J. Energy Chem.*, 2023, **81**, 110-117.
14. H. Yang, L. Wang, Y. Li, Z. Zhuo, T. Wu, J. Liu, L. Xu, H. Du, S. Liu, L. Wu, S. Zhao, M. Tang, W. Yang and H. Yu, *PNAS*, 2024, **121**, e2412460121.
15. W. Huang, C. Lin, J. Qiu, S. Li, Z. Chen, H. Chen, W. Zhao, G. Ren, X. Li, M. Zhang and F. Pan, *Chem*, 2022, **8**, 2163-2178.
16. M. Nakayama, S. Goto, Y. Uchimoto, M. Wakihara, Y. Kitajima, T. Miyanaga and I. Watanabe, *J. Phys. Chem. B*, 2005, **109**, 11197-11203.
17. W. Xiao, Q. Sun, M. N. Banis, B. Wang, W. Li, M. Li, A. Lushington, R. Li, X. Li, T. K. Sham and X. Sun, *Adv. Funct. Mater.*, 2020, **30**, 2000060.
18. Y. Lou, Z. Lin, J. Shen, J. Sun, N. Wang, Z. Chen, R. Huang, X. Rui, X. Wu, H. Yang and Y. Yu, *Adv. Mater.*, 2024, **37**, 2416136.
19. Y. Chen, Y. Zhao, A. Wang, D. Zhang, B. Li, X. He, X. Fan and J. Liu, *Energy Environ. Sci.*, 2024, **17**, 6113-6126.
20. T. Wu, X. Zhang, Y. Li, H. Du, T. Liu, Y. Yang, Z. Zhang, X. Liu, Q. Huang, Y. Ren, J. Qu, S. Zhao, B. Wang, R. Zheng, K. Amine and H. Yu, *Adv. Mater.*, 2024, **37**, 2408543.
21. Y.-H. Zhang, S. Zhang, N. Hu, Y. Liu, J. Ma, P. Han, Z. Hu, X. Wang and G. Cui, *Chem. Soc. Rev.*, 2024, **53**, 3302-3326.
22. P. Kou, L. Zhang, Z. Zhang, R. Zheng, Z. Wang, Y. Wang, Z. Shao, H. Arandiyan, H. Sun and Y. Liu, *Energy Storage Mater.*, 2025, **79**, 104321.
23. Z. K. Tang, Y. F. Xue, G. Teobaldi and L. M. Liu, *Nanoscale Horiz*, 2020, **5**, 1453-1466.

View Article Online
DOI: 10.1039/D6EB00073H

24. A. Van der Ven and G. Ceder, *Electrochem. Solid-State Lett.*, 2000, **3**, 301.
25. A. Van der Ven and G. Ceder, *J. Power Sources*, 2001, **97-98**, 529-531.
26. Y. Huang, Y. Dong, Y. Yang, T. Liu, M. Yoon, S. Li, B. Wang, E. Y. Zheng, J. Lee, Y. Sun, Y. Han, J. Ciston, C. Ophus, C. Song, A. Penn, Y. Liao, H. Ji, T. Shi, M. Liao, Z. Cheng, J. Xiang, Y. Peng, L. Ma, X. Xiao, W. H. Kan, H. Chen, W. Yin, L. Guo, W.-R. Liu, R. Muruganantham, C.-C. Yang, Y. Zhu, Q. Li and J. Li, *Nat. Energy*, 2024, **9**, 1497-1505.
27. S. Tian, S. Liu, H. Du, R. Zhang, Y. Wang, P. Ding, J. Wang, Y. Li, S. Zhao, X. Guo and H. Yu, *ACS Nano*, 2024, **18**, 32065-32076.
28. B. Lelotte, C. A. F. Vaz, L. Xu, C. N. Borca, T. Huthwelker, V. Pelé, C. Jordy, L. Gubler and M. El Kazzi, *ACS Appl. Mater. Interfaces*, 2025, **17**, 14645-14659.
29. Z. Zhuo, K. Dai, R. Qiao, R. Wang, J. Wu, Y. Liu, J. Peng, L. Chen, Y.-d. Chuang, F. Pan, Z.-x. Shen, G. Liu, H. Li, T. P. Devereaux and W. Yang, *Joule*, 2021, **5**, 975-997.

View Article Online
DOI: 10.1039/D6EB00073H

Data availability

The data supporting this article have been included as part of the supplementary information (SI). Supplementary information is available. See DOI: